Available online at www.sciencedirect.com
ScienceDirect
Acta Materialia 55 (2007) 3155–3167
Acta MATERIALIA
www.elsevier.com/locate/actamat

# High-cycle fatigue of nickel-base superalloy René 104 (ME3): Interaction of microstructurally small cracks with grain boundaries of known character

Yong Gao [a], J.S. Stölken [b], Mukul Kumar [b], R.O. Ritchie [a,*]

[a] Department of Materials Science and Engineering, University of California, Berkeley, CA 94720, USA
[b] Lawrence Livermore National Laboratory, Livermore, CA 94550, USA

Received 15 November 2006; received in revised form 29 December 2006; accepted 4 January 2007
Available online 13 March 2007

**Abstract**

High-cycle fatigue (HCF), involving the premature initiation and/or rapid propagation of small cracks to failure due to high-frequency cyclic loading, has been identified as one of the leading causes of turbine engine failures in aircraft. In this work, we consider the feasibility of using grain-boundary engineering to improve the HCF properties of a polycrystalline nickel-base superalloy, René 104 (also known as ME3), through systematic modification of the grain-boundary distribution. In particular, we investigate the growth of microstructurally small fatigue cracks at ambient temperature in microstructures with varying proportions of "special" vs. "random" boundaries, as defined by coincident-site lattice theory. Specifically, we examine the interaction of propagating small (~10–900 μm) surface cracks with grain boundaries of known character, with respect both to any deflection in crack trajectory that occurs at or near the boundary, and more importantly to any local changes in crack-growth rates. In addition, finite-element calculations are performed to evaluate the effective driving force and plastic-zone profile for such small-crack propagation, incorporating information from both the local microstructure (from electron backscattering diffraction scans) and the surface crack-path profile.


*Keywords:* High-cycle fatigue; Grain-boundary engineering; Fatigue thresholds; Small cracks; Superalloys

## 1. Introduction

The control and prevention of failures due to high-cycle fatigue (HCF) in turbine engine components represents a problem of considerable importance for civilian and particularly military aircraft [1–3]. Such failures result from the initiation and growth of small cracks that propagate rapidly to critical size, driven by high-frequency (>1 kHz) vibrational loads. In conventional gas-turbine engines, the highest temperature components are invariably made of nickel-base superalloys, materials which have been studied extensively to improve their fatigue properties through compositional and microstructural design. However, the question as to whether these microstructures can be optimized to specifically promote high-cycle fatigue resistance has rarely been addressed.

In the HCF regime, the vast majority of the life is spent in the initiation and early propagation of small cracks,[1] typically of a size in the range of few to hundreds of micrometers. In gas-turbine components such as blades and disks, such small cracks generally initiate from small defects resulting from fretting and domestic-/foreign-object damage [3]; moreover, they can grow at rates in excess of

* Corresponding author. Tel.: +1 510 486 5798; fax: +1 510 486 4881.
*E-mail address:* roritchie@lbl.gov (R.O. Ritchie).

[1] Small cracks may be defined as being (i) microstructurally small, i.e., small compared to microstructural dimensions, (ii) mechanically small, i.e., small compared to the scale of local plasticity (e.g., the plastic-zone size), or (iii) functionally small, i.e., small compared to the extent of crack-tip shielding (e.g., crack closure) in the crack wake. Additionally, unlike short cracks, small cracks are assumed to be small in all dimensions.

1359-6454/$30.00 
doi:10.1016/j.actamat.2007.01.033

corresponding (steady-state) large cracks at the same nominal stress intensity $\Delta K$ levels, and further can propagate at stress-intensity ranges less than the fatigue threshold, $\Delta K_{TH}$ [4–6], below which large cracks are presumed to be dormant. The mechanistic nature of their initiation and growth depends upon several factors, including the purity, grain size and slip planarity of the alloy, the temperature and environmental conditions, and mechanical factors such as load ratio and frequency [4–8].

Cracks of this size-scale are known to be locally affected by interactions with microstructural features of comparable dimensions [6,9]. Specifically, once crack sizes approach the characteristic scale of the microstructure, the role of grain boundaries in particular may become far more critical, for example in acting as local arrest barriers to small crack growth [5,9,10]. In the present study, we examine the specific interaction of growing small fatigue cracks with boundaries of known character. The rationale for the latter process is to induce grain-boundary engineering, which is known in specific instances to enhance microstructural resistance to fracture [11]. In general, this involves changes to the grain-boundary character distribution, mainly by promoting higher fraction (and higher degree of connectivity) of "special" grain boundaries that exhibit special misorientations and a high degree of atomic matching, as described by the coincident-site lattice model [12].[2] In terms of fracture resistance, the main effects of such an increase in the fraction of such "special' boundaries have been associated with intergranular fracture, specifically involving stress-corrosion cracking, creep and cavitation behavior [14–23]. The effect of an increasing "special' fractions on fatigue fracture, where fractures are often transgranular, is far less clear. There have been only a few reports on the effect of boundary character on fatigue. An initial study [24] found that the ambient-temperature, smooth-bar, tension–tension fatigue lives for two $\gamma/\gamma'$ superalloys were increased by a factor of ~1.5 in an Fe-base alloy by increasing the "special" fraction from 20% to 65%, and by a factor of 3 in a Ni-base alloy by increasing this fraction from 9% to 49%, although no mechanistic explanations were proposed. A second study on the Ni-base $\gamma/\gamma'$ superalloy ME3 by the current authors [25] showed that increases in the "special" fraction from 29% to 42% (at a constant ~15 μm grain size) had little effect on resistance to the growth of large (~8–20 mm) cracks at ambient temperature, where crack growth was predominantly transgranular. However, at elevated temperatures (700–800 °C) where crack paths were ~30–75% intergranular, grain-boundary engineering was found to diminish the fraction of intergranular cracking by as much as 25% with a concomitant improvement in the fatigue threshold by 10–20%. This work demonstrated that for cracks large compared to the scale of the microstructure, the principal role of an increased fraction of "special" boundaries is to enhance resistance only to intergranular cracking. The question that remains, however, is whether such "special" boundaries can provide an improved barrier to the motion of transgranular cracks when crack sizes are microstructurally small.

Accordingly, in this work, we first examine the role of an increased fraction of "special" grain boundaries on the fatigue-crack growth behavior of small (~10–900 μm) surface cracks in the as-received and grain-boundary-engineered ME3 superalloy, and then further investigate how specific grain boundaries of known character can locally affect the propagation of these small cracks, both in terms of their trajectory and growth rate. Large-scale finite-element (FE) calculations are performed to discern whether the observed variations in small-crack growth rates are caused by local changes in the crack-growth resistance or are the result of fluctuations in the effective (local) crack-driving force.

## 2. Procedures

### 2.1. Material

Studies were performed on the powder-metallurgy nickel-base superalloy, ME3 (also known as René 104), a polycrystalline Ni–Co–Cr alloy, similar to Udimet 720, designed to have extended durability at 650 °C for aircraft engine disk applications by utilizing a moderately high $\gamma'$ precipitate content with high refractory element levels. Forged heats of the alloy were received as plate stock from NASA Glenn (as-received), with equiaxed matrix grain sizes, $D_g$, of 15 μm. An additional heat was obtained from GE Aircraft Engines with a much smaller grain size of $D_g \sim 1.3$ μm. Both as-received microstructures comprised a bimodal distribution of ~20 and 100–200 nm ordered $\gamma'$ ($L1_2$) precipitates within the equiaxed $\gamma$ matrix. Typical ambient and elevated temperature mechanical properties are listed in Table 1 [26].

### 2.2. Thermomechanical treatments

As-received plate-stock (300 mm in diameter) was electrical-discharge-machined into small segments for thermomechanical processing. Grain-boundary engineering using strain and high-temperature annealing of the single-phase material was achieved using the following schedule [25]: (a) as-received sections were first solutionized at 1175 °C for 2 h and then air-cooled to dissolve the $\gamma'$ precipitates, (b) microstructures were then grain-boundary-engineered using four cycles of cold rolling (10% reduction in thickness per cycle) followed by a 30 min anneal at 1150 °C in an air furnace, before (c) a final duplex aging treatment (4 h at 843 °C, followed by 8 h at 760 °C) was carried out to re-

[2] "Special" boundaries are described geometrically by having a low "sigma number", $\Sigma(1 < \Sigma \leqslant 29)$, which is defined in terms of the coincident-site lattice model [12] as the reciprocal of the fraction of lattice points in the boundaries that coincide between the two adjoining grains, with an allowable angular deviation from the Brandon criterion of $\Delta\theta = 15° \cdot \Sigma^{-1/2}$ [13].

Table 1
Mechanical properties of the as-received ME3 alloy at ambient temperature

| Heat | Yield strength (MPa) | Tensile strength (MPa) | Reduction in area |
|---|---|---|---|
| As-received | 1150 | 1650 | 21% |

precipitate the $\gamma'$ as a bimodal distribution of cuboidal precipitates. The resulting (GB-engineered) microstructures (from either the fine- or coarse-grained heats) had an equiaxed matrix grain size of $D_g \sim 13$ μm.

Additionally, certain as-received samples were annealed at 1175 °C for 5 h (followed by air cooling and duplex aging, as above) to promote grain growth without modifying the fraction of special boundaries; these (grain-coarsened) microstructures had an equiaxed matrix grain size of $D_g \sim 25$ μm. Both the grain-boundary engineering and grain-coarsening treatments did not change the crystallographic texture, as described elsewhere [25].

### 2.3. Small crack initiation and propagation

Examination of the crack-growth behavior of small cracks was conducted at ambient temperature on ~10–900 μm long surface cracks, initiated on the top (tension) surface of 1.8 mm thick rectangular-beam specimens (40 mm long, 2.8 mm wide), loaded in four-point bending. The four-point bending test was chosen because it provides a uniformly stressed top surface between the inner two loading points. Samples were cycled in room air (25 °C), under load control, with maximum surface stress between 75% and 95% of the yield stress, $\sigma_y$, at load ratio (ratio of minimum to maximum loads) of $R = 0.1$ and at a cyclic frequency between 25 and 50 Hz (sine wave). Prior to fatigue testing, the top surfaces of the specimens were polished to a 0.05 μm finish with colloidal silica and subsequently electropolished (acetic acid:perchloric acid ~3:1 for 5 s at 5 V) to facilitate monitoring of the surface crack behavior.

In order to determine the appropriate stress level for controlling small crack initiation and propagation as well as further examine the grain-boundary engineering effect, stress-life $S$–$N$ tests were first conducted on as-received (fine: $D_g \sim 1.3$ μm and coarse: $D_g \sim 15$ μm) and GB-engineered ($D_g \sim 13$ μm) microstructures with the same specimen geometry in four-point bending ($R = 0.1$, frequency = 50 Hz, room temperature).

#### 2.3.1. Crack initiation

Fatigue cracks were initiated either naturally or from artificially introduced flaws, specifically focused-ion beam (FIB) milled micronotches and Vickers microhardness indents. Natural initiation was defined in the optical microscope (OM) by the first appearance of a surface crack of length ~10–30 μm, whereupon the loads were reduced in order to monitor its growth. The micronotches were diamond-shaped with a depth of ~20–50 μm; these notches were assumed to be relatively strain-free as the localized etching with FIB irradiation was achieved with a low current (starting at ~1000 pA, finishing at ~100 pA) gallium ion beam. Microhardness indents of similar dimension (diagonal length ~20 μm) were also used; however, despite the surrounding residual tensile field, cracks never initiated at these indents.

#### 2.3.2. Crack propagation

Measurements of the small crack growth rates were made with periodic replication, using cellulose acetate tape softened with acetone, of loaded samples every ~$3–5 \times 10^4$ cycles throughout the test. Corresponding crack lengths were measured from these replicas using optical microscopy, with growth rates computed from the amount of crack extension (~1–10 μm) between two discrete measurements (replicas). Stress intensities were determined from the linear-elastic solutions for surface cracks in bending [27]. A semi-elliptical crack profile, i.e., a crack depth to half-surface length ratio of $a/c \sim 2/3$, was assumed, based on experimental measurements of the shape of the crack

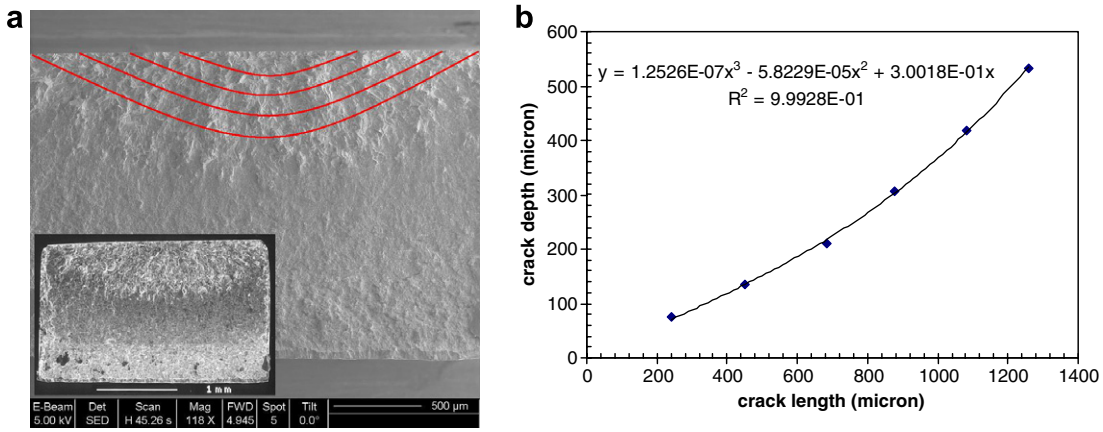


Fig. 1. (a) SEM fractographs of small fatigue crack-growth showing a semi-elliptical crack profile, indicated by the red contour lines; also shown in bottom left corner, is an overview of the broken specimen. (b) Polynomial relationship between the crack depth $a$ and crack length $2c$. (For interpretation of the references to colour in this figure legend, the reader is referred to the web version of this article.)

in broken samples. One such crack is shown in Fig. 1, where the radial marks on the fracture surface, which indicate successive positions of the crack front, have been highlighted; it is apparent that crack advance is more rapid at the surface than depthwise. Results are presented in terms of surface crack-growth rate, $dc/dN$, as a function of the stress-intensity range, $\Delta K$, and are compared with our previous measurements of the growth rates of large (~8–20 mm), through-thickness cracks in the ME3 superalloy in the same microstructures.

For all tests and conditions, the specimen thickness $B$ and width $W$, were always large compared to the maximum plastic-zone size, estimated by $r_{y,max} \sim 1/2\pi(K_{max}/\sigma_y)^2$, where $K_{max}$ is the maximum stress intensity in the fatigue cycle; specifically, $B$, $W > 15r_{y,max}$, implying that small-scale yielding (SSY) conditions prevailed throughout.

### 2.4. EBSD characterization

Electron backscattering diffraction (EBSD) measurements were made by orientation mapping of metallographically prepared specimens in a Philips XL-30S scanning electron microscope (SEM) equipped with the OIM™ software from TSL, Inc. (Draper, UT). Analysis of the EBSD data were performed using custom algorithms described in detail elsewhere [28–30]. Grain boundaries were categorized according to the coincident-site lattice model and the Brandon criterion [12].

### 2.5. Numerical calculation procedures

Numerical calculations were performed to discern whether the observed crack-growth rate variations resulted from local changes in the intrinsic microstructural resistance or from fluctuations in the effective crack-driving force. For example, an explanation for the growth-rate variations could be that the local grain structure modulates variations in elastic and plastic anisotropy, thereby mediating the effective driving force for crack growth. To test this hypothesis and estimate local changes in driving force, finite-element simulations that directly incorporated the observed crack geometry and microstructure were performed. The driving force estimated from these simulations was then compared to that derived from an analytic solution to obtain a local correction or shielding factor for a given crack geometry and microstructure.

A precise solution for the local driving force around the crack front of a three-dimensional surface flaw requires extraordinary computing work and a sequence of two-dimensional EBSD maps from serial-sectioning experiments, which was not available in this study. Accordingly, the complex three-dimensional nature of the crack path and microstructure was approximated by considering only the free-surface region under plane-stress loading. We believe that such a two-dimensional approximation is justified by examining the variation in local applied stress intensity $\Delta K$ with position along the two-dimensional crack front [25], which reveals that the largest values of $\Delta K$ exist at the surface. The specific model comprised a two-dimensional surface slice containing an irregular crack under tensile loading, i.e., as a nominal middle-cracked tension specimen (termed the "numerical specimen"). The stress-state at the surface of the beam was then well approximated by a state of pure tension applied in the numerical model. The small crack size in relation to the beam precluded the simulation of the entire width of the beam; the demands of high mesh resolution and large sample size would result in a computationally prohibitive multi-million-element simulation. For this reason the width of the numerical specimen was fixed to be twice as long as the longest crack considered. This choice ensured that the plastic zone was well contained within the specimen, thereby simplifying $J$-integral calculations.

The detailed crack geometry and local microstructure were incorporated using the result of the EBSD scans and crack-growth measurements to explicitly represent the crack and grain-structure in a high-resolution finite-element mesh, shown in Fig. 2. A single-crystal plasticity constitutive description was used to account for local variations in elastic and plastic anisotropies. The crystal plasticity yield strength and hardening parameters were chosen to be consistent with the experimentally determined values for the bulk specimen. The size of the surface region that was scanned using EBSD was too small to model directly as a middle-cracked tension specimen. To remedy this, the EBSD data (or "EBSD mesh") was extended to form the numerical specimen. The extended region was modeled using a single crystal plasticity description, the elastic properties of which were derived by calculating the uncracked effective moduli of the region scanned by EBSD through direct numerical simulation under plane-stress loading. This choice eliminates, on average, the elastic mismatch between the uniform mesh region containing the high-resolution orientation data and the regions where the mesh is extended. The mismatch in plastic properties between the EBSD mesh region and the surrounding extended region was rendered benign in that the plastic zone in the cases considered was contained completely in the uniform EBSD mesh region.

The finite-element analysis was performed using the ALE3D code developed at the Lawrence Livermore National Laboratory. The EBSD data were processed and suitably averaged [31] to obtain the effective crystal orientation for each element of the mesh. The EBSD data extend over a mesh region of $\sim 293 \times 1041$ μm, with a uniform element size of $1.25 \times 2.15$ μm. The individual crystal grains and crack geometry were resolved to a scale of ~1.6 μm, resulting on average in ~50 finite elements per grain and a crack length resolution of ~2 μm. The geometry of the crack was modeled by selectively removing material from this uniform field of crystal orientation data, resulting in a "digitized" crack geometry. The crack was primarily one element wide (1.25 μm), except in regions where the crack ran diagonally to the mesh, where it was

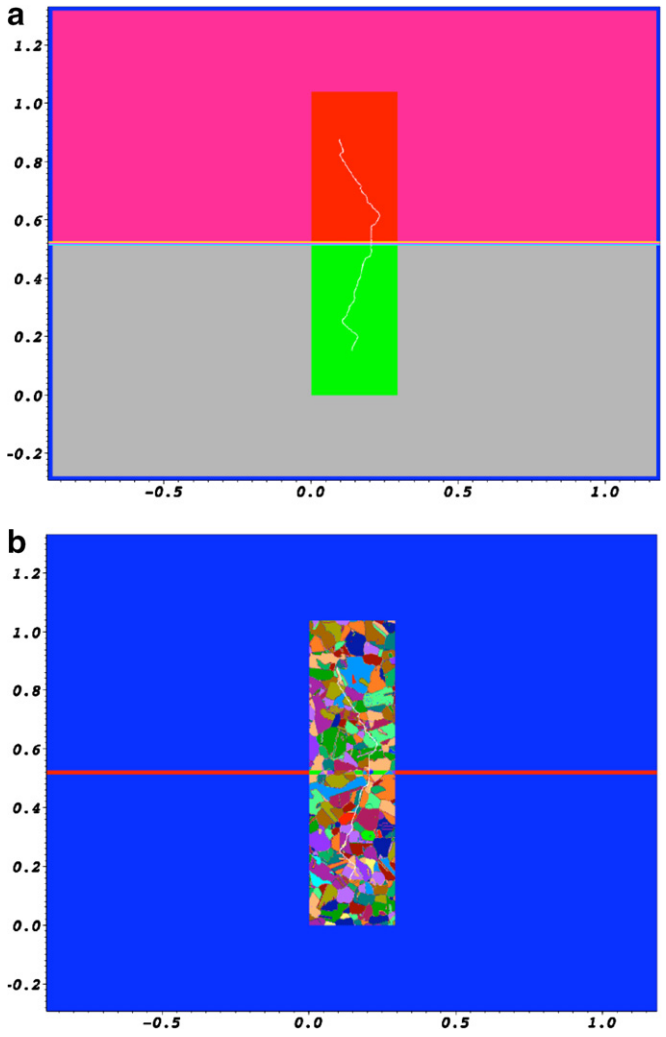


Fig. 2. (a) Finite-element computational zones showing region of embedded crack data from the EBSD data and regions used to calculate the upper and lower *J*-integrals (scale in mm); (b) finite-element material zones showing region of EBSD data embedded in the "numerical middle-cracked tension" specimen (scale in mm).

then typically double this width. This approach was adopted to facilitate crack reconstruction at various stages of crack growth while maintaining a consistent finite-element mesh and crystal orientation distribution. The uniform mesh region spanned by the EBSD data were not large enough to accommodate the numerical specimen of the desired size and thus was extended both laterally and vertically to a size of $2.079 \times 1.624$ mm with the resulting finite-element simulation consisting of over 490,000 degrees of freedom.

Simulations were performed corresponding to six different crack lengths (between 400 and 820 μm) where significant changes in the crack-growth rate were observed experimentally. A uniform tensile stress was applied such that, for the longest crack considered, the applied $\Delta K$ for a straight crack in the numerical sample was equal to that at the surface of the experimental bend beam, where the analytical solutions under conditions of small-scale yielding were used in both cases. The stress level (400 MPa) from this long-crack limit calibration was then fixed for all six simulations. This ensured that the applied $K$ for a given crack length in the numerical specimen was comparable to the estimated value for the same crack length; in most cases, the simulated applied $\Delta K$ was within 6% of the experimentally estimated value. The simulated stress and strain fields under quasi-static loading were then used to calculate the values of the *J*-integral [32] for both the upper and lower cracks. The value of the *J*-integral ($J_{FE}$) calculated from the finite-element simulation was then compared to the *J*-integral ($J_{SSY}$) estimated from the analytic solution of a straight crack under the same conditions of loading under the assumptions of small-scale yielding. To facilitate comparison with experiment, the values of $J_{FE}$ and $J_{SSY}$ were expressed in terms of equivalent $K_{FE}$ and $K_{SSY}$. The ratio of $K_{FE}$ and $K_{SSY}$ calculated for a given crack configuration and applied loading of the numerical specimen was then used to correct the estimate of the applied $\Delta K$ (namely, $\Delta K_{cor} = \Delta K \cdot (K_{FE}/K_{SSY})$) in the small-crack experiment corresponding to the same crack configuration and apparent loading ($K_{SSY}$).

## 3. Results

### 3.1. Grain-boundary-engineered microstructures

EBSD results on the grain-boundary character distribution and texture of the as-received and grain-boundary-engineered microstructures indicated that the (number) fraction of special grain boundaries, $f_N$, was enhanced by over 40% by the thermomechanical processing; specifically $f_N$ was increased from 0.28 to 0.41. Additionally, the length fractions ($f_L$) of special boundaries were correspondingly increased from 0.38 to 0.56.[3] Additional EBSD scans verified that these microstructures were isotropic regardless of the plane of observation.

With the increase in the special fraction, there was also a marked reduction in the fraction of triple junctions that are coordinated with three crystallographically random boundaries ($\chi_0$).[4] In addition, over 95% of the random boundaries in the as-received microstructures were in clusters larger than 500 grain diameters, which implies that the network of random boundaries was infinite in extent. This percentage was reduced to zero in the grain-boundary-engineered microstructures, indicating that an infinitely percolating network of random boundaries did not exist in the engineered microstructures, even with only a modest enhancement in the fraction of special boundaries.

All microstructures showed no change in hardness (Rockwell C ~ 44) after processing. Additionally, they dis-

[3] The disproportionate increase in the length fraction in comparison with the number fraction is entirely due to the increased frequency of lower energy special boundaries such as annealing twins (Σ3).

[4] $\chi_n$ refers to the fraction of triple points that have $n$ special boundaries, where $n = 0$, 1, 2, or 3.

played very low texture, i.e., ~1.5–1.7 times random, with a minimal ⟨1 1 1⟩ component; this can be categorized as weak to no texture but is indicative of a face-centered cubic (fcc) alloy with low stacking-fault energy. This texture was unchanged by grain-boundary engineering.

### 3.2. Stress-life (S/N) behavior

The results of the stress-life ($S/N$) tests, performed in 25 °C room air at $R = 0.1$, are shown for the as-received and grain-boundary-engineered microstructures in Fig. 3. These data show high $10^8$-cycle endurance strengths for this alloy between ~950 and 1050 MPa. At a nominally fixed grain size, the GB-engineered microstructure does show slightly higher (2–3%) fatigue endurance strength than the corresponding as-received microstructure. However, the most significant effect is that the finer-grained microstructure displays the superior fatigue life properties, with an endurance strength some 4–7% higher than that of the coarser-grained microstructures. Interestingly, this is exactly the opposite of the ranking of these microstructures when evaluated for large crack growth resistance [25].

### 3.3. Small crack growth-rate behavior

The variation in crack-growth rates of the small (~10–900 μm) surface fatigue cracks in both the as-received and grain-boundary-engineered microstructures is shown as a function of the stress-intensity range, $\Delta K$, in Fig. 4; results are compared with previous results [25] for the growth of large (~8–20 mm) through-thickness cracks in the same microstructures. Although small crack-growth rates are characterized by excessive scatter due to local interactions with features in the microstructure of comparable dimensions, below $\Delta K \sim 14\ \mathrm{MPa}\sqrt{\mathrm{m}}$ growth rates are definitively higher than those of equivalent large cracks and further propagate at stress-intensity ranges well below the large-crack thresholds, i.e., as low as 5–6 $\mathrm{MPa}\sqrt{\mathrm{m}}$. With continued propagation at higher $\Delta K$ levels $\sim 18\ \mathrm{MPa}\sqrt{\mathrm{m}}$, large and small crack-growth rates tend to merge. However, it is apparent that similar to the behavior of large cracks [25], at ambient temperatures where crack advance is mostly transgranular, there is little discernable overall effect of an increased fraction of special boundaries on the growth rates of small cracks in this alloy.

### 3.4. Interaction of small surface crack and grain boundaries of known character

To examine how such small cracks interact with individual grain boundaries of specific character, studies were performed on small (10–900 μm) surface cracks in the grain-coarsened microstructure (with an equiaxed matrix grain size of ~25 μm). The results of one such test are plotted in Fig. 5; here the variation in stress-intensity range and corresponding local crack-growth rates for a micronotch-initiated small crack are shown as it encounters numerous grain boundaries during cycling under a constant alternating load (the maximum surface stress was ~82% of the yield stress). Note that cracks initiated at the tips of the diamond-shaped micronotch and extended, both left and right, along a path normal to the external cyclic loads at a nominally increasing growth rate as the $\Delta K$ values increases (with crack advance) from $\sim 6$ to $18\ \mathrm{MPa}\sqrt{\mathrm{m}}$. Also shown are optical micrographs of the crack and grain structure, the latter characterized using EBSD analysis to define the nature of each intercepted grain boundary; the random grain-boundary network is enhanced in yellow

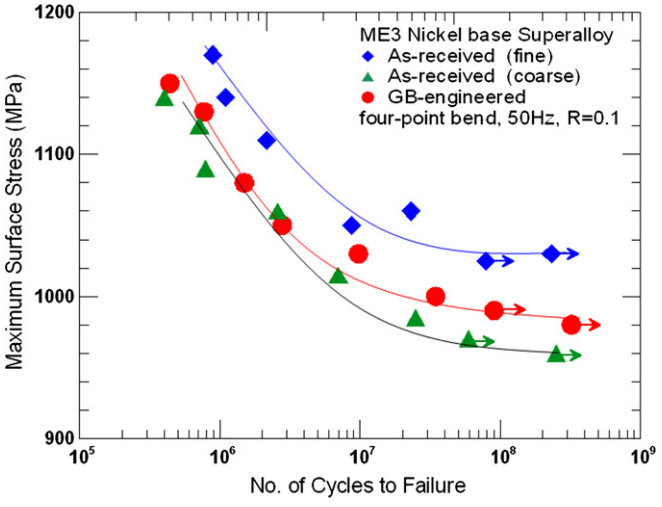


Fig. 3. Stress/life (S/N) curves (in 25 °C room air at $R = 0.1$, 50 Hz) for the nickel-base superalloy ME3 in three microstructural conditions: as-received (fine grained: $D_g \sim 1.3$ μm, coarse grained: $D_g \sim 15$ μm) and GB-engineered ($D_g \sim 13$ μm).

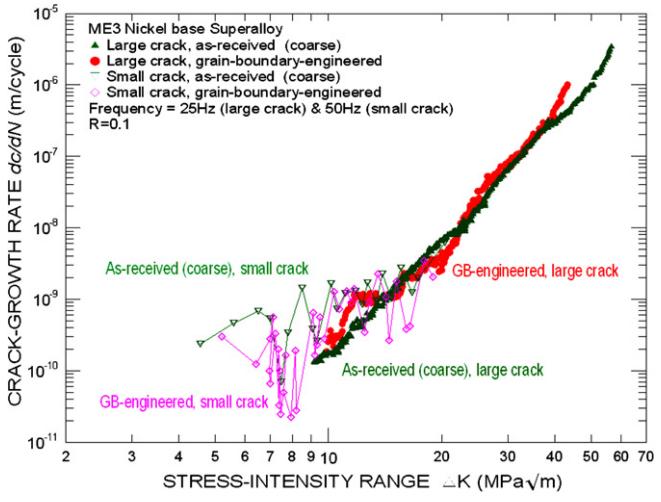


Fig. 4. Variation in fatigue-crack propagation behavior for small (~10–900 μm) surface cracks in the as-received (coarse-grained) and GB-engineered microstructures of ME3 (with approximately constant grain size of 13–15 μm). Testing performed in four-point bending at $R = 0.1$ at 50 Hz frequency in 25 °C room air. Results are compared to corresponding data on the propagation of large (8–20 mm) through-thickness cracks in the same microstructures, as described in Ref. [25].

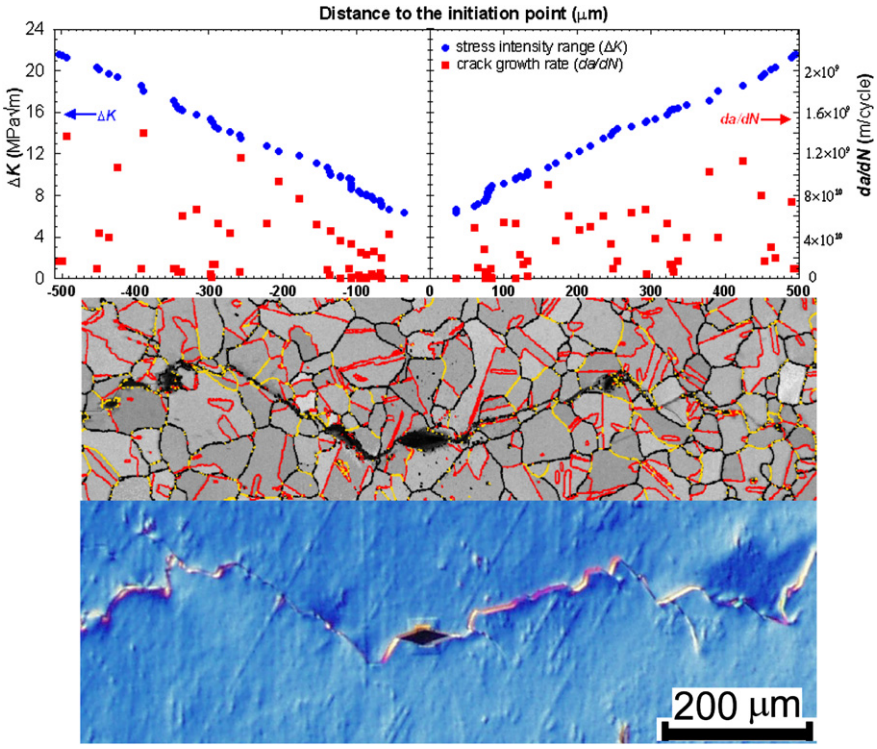


Fig. 5. Variation in fatigue-crack propagation behavior for small surface cracks in the grain-coarsened ME3, together with EBSD characterization of the path for small crack propagation. Random boundaries are shown as black lines twin boundaries are in red, other special boundaries are in yellow.

and the special grain boundaries are shown in red (representing $\Sigma 3$ (twin) boundaries) and blue (representing other $\Sigma 3^n$ special boundaries).

Akin to large-crack growth at ambient temperatures [25], the surface crack path was predominantly (but not exclusively) transgranular and facetted in nature. Where the crack went intergranular (less than 10%), both random and special boundaries were sampled in approximately equal proportions. The facetted nature of the crack path can also be seen from the SEM images of the fracture surfaces in Fig. 6, where it is apparent that the tortuosity results from the crystallographic crack growth along favored slip planes in the $\gamma$ matrix, and from deflection at grain boundaries due to the orientation between the adjoining grains. As expected, the crystallographic crack path was preferably along {1 1 1} planes; this is evident as the crack often extended along, or parallel to, the $\Sigma 3$ (twin) boundaries, which are invariably {1 1 1} in fcc metals (Fig. 7). Several such profiles were analyzed; some where the crack was allowed to initiate naturally, as shown in Fig. 8, where crack nucleation can be seen to occur at a triple junction composed of three random grain boundaries.

To quantify how the specific boundaries, characterized by their grain-boundary misorientation angle ($\theta$), affect the motion of the crack, further experiments of similar nature were performed. As the growing crack encountered each boundary of differing misorientation, both the crack-deflection angle ($\Delta\phi$) and change in local growth rates ($\Delta dc/dN$) were determined and an average calculated based on several measurements. Specifically, an assessment of the deflection of the transgranular crack path was made by measuring average crack-deflection angles, defined as

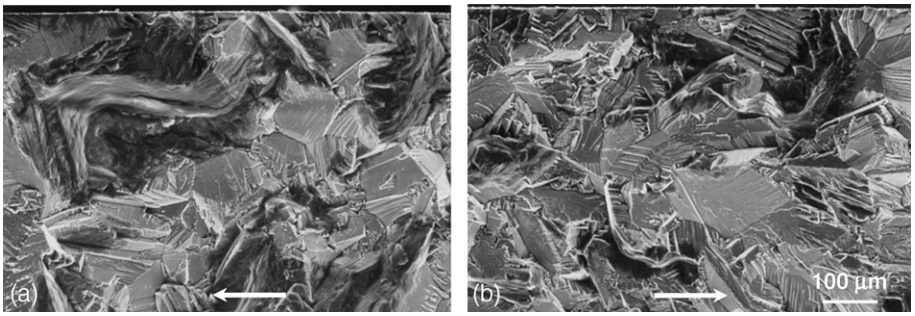


Fig. 6. SEM fractographs of small-crack growth in the grain-coarsened ME3 alloy, showing the facetted nature of the crack path at the early propagation stage. Both (a) and (b) are ~200–300 μm from the crack-initiation site. (White arrows indicate the crack-propagation direction, which is normal to the externally applied stresses.)

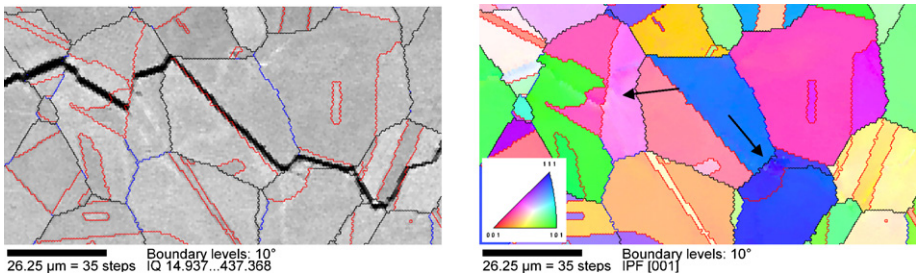


Fig. 7. EBSD images showing crystal rotation due to local plasticity as cracks impinge at grain boundaries and are then deflected. Crystallographic crack path is preferably along {1 1 1}, i.e., crack tends to extend along, or rather close to, Σ3 twin boundaries. Examples are shown by arrows where the crack impinges the grain boundaries and then gets deflected. The plastic zone extends into the neighboring grain ahead of the deflected crack.

the difference in angle between crack path before and after impingement at the boundary (as shown in Fig. 9). In addition, the perturbation in crack-growth rate was measured, in terms of the change in growth rate at the grain boundary from the average crack-growth rate (average of 2–4 measurements) in the neighboring grains before and after impingement (Fig. 10). The grain-boundary misorientation angle was obtained directly from the EBSD analysis.

Although there is considerable scatter in the data, a general trend of higher crack-deflection angles may be deduced for boundaries with larger degrees of misorientation (Fig. 9); the behavior of special boundaries does not appear to be radically different from that of random boundaries in this regard. In terms of growth rates (Fig. 10), the data suggest that grain boundaries locally retard crack extension and that special boundaries are no more effective than random boundaries. There is, however, a general trend of increased retardation at boundaries with larger misorientation angles, with the $\Sigma 3(\theta \sim 60^\circ)$ twin boundaries providing some of the largest crack-growth retardations.

### 3.5. Finite-element calculations of local crack-driving forces

The experimental studies described above were focused on observing the growth of cracks propagating in an inhomogeneous material of varying local elastic–plastic anisotropy. To characterize this growth, a driving force ($\Delta K$) is conventionally estimated by ignoring these local variations, on the assumption that such changes in crack geometry and material properties are both small compared to the crack size and the scale of the fracture process zone, respectively. However, it is unclear to what extent such local variations in crack geometry and elastic–plastic anisotropy affect the conventional estimates of driving force when applied to the current situation of a propagating small crack. Two-dimensional finite-element simulations that directly incorporate local geometric and material property variations into estimates of crack-driving force were performed and compared to conventional global crack estimates (from handbook $K$ solutions) that assume idealized geometry (straight and planar crack surface) and isotropic material parameters.

Several observations regarding the observed crack-growth rate and the corrected stress-intensity range $\Delta K_{cor}$ can be made. For a given crack length, the true driving force $\Delta K_{cor}$ at the crack tips on both sides was not same; indeed, sometimes there was a considerable difference, as much as 16% (refer to the crack length 726 μm in Table 2), as shown in Table 2 (Fig. 11). Taken as a whole, there is a moderate correlation in crack-growth rate with $\Delta K_{cor}$ for the twelve cases considered (six simulations, two crack tips each). There is a strong correlation of crack-growth

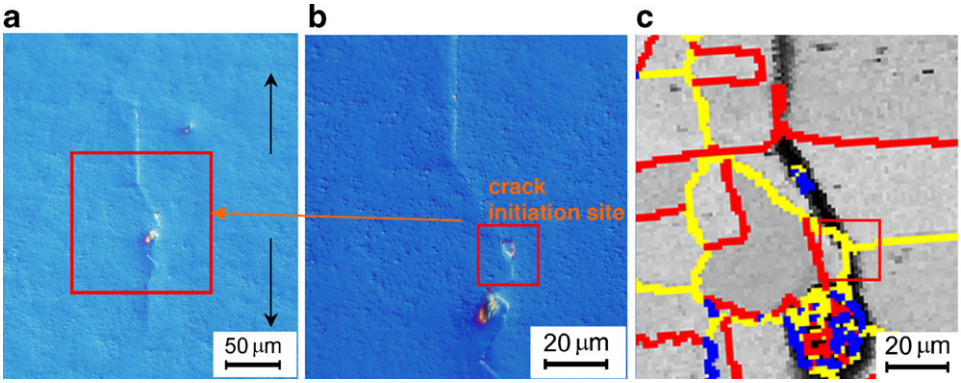


Fig. 8. Crack nucleation site in Fig. 6 showing initiation at triple junction of three random grain boundaries: (a) low-magnification OM image, (b) higher-magnification OM image, and (c) EBSD picture showing the same crack initiation position. Random boundaries are shown as yellow lines; twin boundaries are in red, other special boundaries are in blue. (Black arrows indicate the crack-propagation direction, which is normal to the externally applied stresses.)

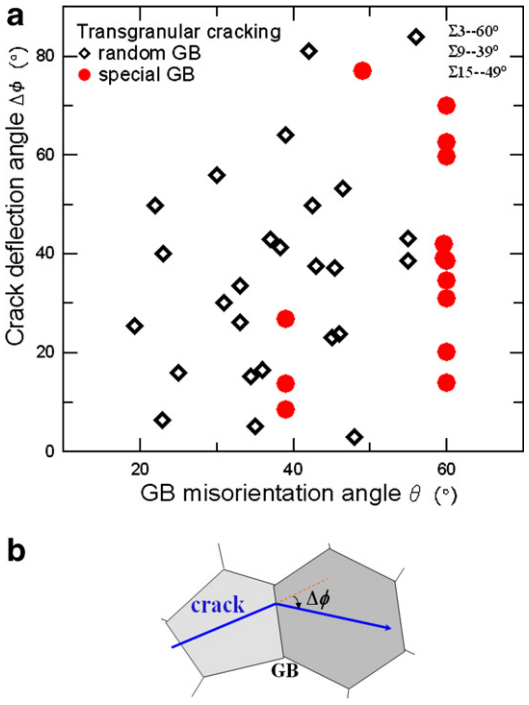


Fig. 9. Experimentally measured variation in average crack-deflection angle with the grain-boundary misorientation angle ($\theta$) for the transgranular propagation of small surface cracks as they encounter grain boundaries of known character in the grain-coarsened microstructure. A general trend of higher crack-deflection angles associated with boundaries with larger degrees of misorientation is seen. (b) Schematic illustration showing how the change in crack-deflection angle ($\Delta\phi$) was calculated.

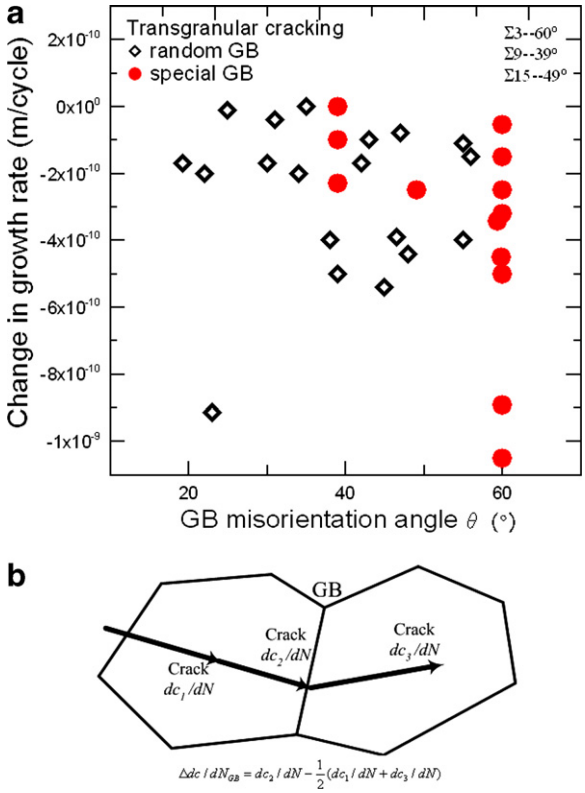


Fig. 10. (a) Experimentally measured variation in average crack-growth rates ($\Delta dc/dN$) with the grain-boundary misorientation angle ($\theta$) for the transgranular propagation of small surface cracks as they encounter grain boundaries of known character in grain-coarsened microstructures. A general trend of higher crack-growth retardation associated with boundaries with larger misorientation angles is seen. (b) Schematic illustration showing how the change in crack-growth rates ($\Delta dc/dN$) was calculated for the process of a crack propagating through a grain boundary.

rate with $\Delta K_{cor}$ with the exception of the very low growth-rate data on the left side of the crack, especially the two data sets (as indicated in those connected three data points in each set shown in inset of Fig. 11) on the right-hand side where the crack-growth rates can be well associated with corrected intensity range $\Delta K_{cor}$ and crack-deflection events (the detail of the crack-profile also shown in Fig. 5 and simulated in Fig. 12). The deflection events appear to occur when the crack tip is in the vicinity of a grain boundary and at triple junctions (Fig. 12). Although the growth rate may vary by a factor of two or so as the crack propagates across various features such as grain boundaries, it is in the neighborhood of triple junctions that gross crack deflection and an associated order of magnitude decrease in crack-growth rate are well correlated.

## 4. Discussion

In contrast to most studies on the effect of grain-boundary engineering on fracture, which have focused on intergranular cracking, the present work has examined how grain-boundaries affect the predominantly transgranular propagation of cracks. Specifically, the interaction of microstructurally small cracks with boundaries of known character has been monitored in a $\gamma/\gamma'$ nickel-base superalloy, where the mode of crack advance is predominantly

Table 2
Calculation of the corrected crack-propagation driving force from finite-element simulations as compared to standard analytical solutions

| Crack length (μm) | $K_{FE}$ (left/right) (MPa$\sqrt{m}$) | $K_{SSY}$ (MPa$\sqrt{m}$) | $\Delta K$[a] (MPa$\sqrt{m}$) | $\Delta K_{cor}$ (left/right)[b] (MPa$\sqrt{m}$) |
|---|---|---|---|---|
| 408 | 10.83/11.30 | 10.99 | 12.2 | 12.02/12.54 |
| 504 | 12.22/10.99 | 12.75 | 13.8 | 13.23/11.90 |
| 564 | 14.54/13.59 | 13.90 | 14.6 | 15.27/14.27 |
| 726 | 16.67/19.76 | 17.67 | 17.1 | 16.13/19.12 |
| 780 | 17.08/19.05 | 19.26 | 18.0 | 15.96/17.80 |
| 817 | 18.27/20.58 | 20.34 | 18.55 | 16.66/18.77 |

[a] Determined analytically from handbook solutions [25].
[b] Computed for each end (left/right) of the crack using the finite-element analysis.

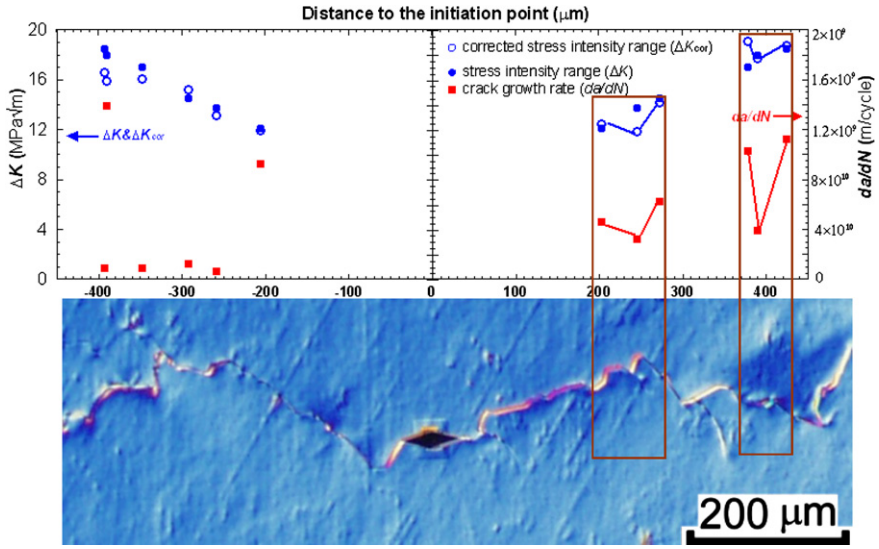


Fig. 11. Relationship between the measured crack-growth rates and numerically corrected applied $\Delta K_{cor}$, calculated from the finite-element simulation, together with an optical microscopy characterization of the path of the small crack (similar to Fig. 5). It should be noted that there is a good correlation between these parameters, suggesting that variations in crack-growth rate are not due to changes in driving force.

crystallographic in nature (along favored {1 1 1} slip planes).

As the crack-tip plastic-zone size for these small cracks becomes comparable to the length scale of the grain size, different misorientations across grain boundaries along the crack path, as well as the anisotropy of elastic and plastic behavior, are likely to play a key role in governing crack-growth behavior. Based on several studies on the fatigue of fcc materials [33–35], it is known that the local crystallographic orientation of a crack can have an important effect on small crack growth. A tendency toward planar slip on the crystallographic planes, principally {1 1 1}, but also {1 1 0} and {1 0 0}, has been reported, which is confirmed by the crystallographic facets along {1 1 1} planes observed in the present study. As the boundary misorientation between adjacent grains typically contains both the tilt and twist components, this can further lead to the crack deflection and retardation. Additionally, the crack can leave a ligament when traversing a twist boundary, which can increase the retardation as it must be subsequently fractured [33].

In the present work, on small surface cracks that are propagating transgranularly and impinging on grain boundaries, our experimental studies indicate that there is a tendency for the degree of deflection and the magnitude of the crack-growth retardation to be increased with increase in the crystallographic misorientation across the boundary (Figs. 9 and 10). There is considerable scatter in the growth-rate measurements, of course, but these results do suggest that special and random boundaries are comparable in their effect in perturbing the transgranular progress of small cracks. However, our data also show that $\Sigma 3$ twin boundaries (where $\Delta\theta \sim 60°$) are a particularly effective means of slowing down the progress of small cracks, and this may present a reason for employing grain-boundary engineering for high-cycle fatigue resistance. We have shown previously [25] that an increased fraction of special boundaries can lead to higher long-crack fatigue thresholds at elevated temperatures (700–800 °C in MP3) by acting to diminish the role of intergranular cracking. We now show that this increased special fraction, by virtue of the resultant increase in the fraction of twin boundaries, can also enhance the resistance to transgranular small crack growth, although it must be stated that, quantitatively, both effects are not large.

In addition to the character of the boundaries, it appears that the presence of multiple grains near the crack tip has a strong influence on the proclivity for crack deflection and the reduction of the crack-growth rate (Fig. 12). Closer examination of these finite-element results indicates that, when a crack tip resides predominantly within one grain, the plastic zone (within a 200 μm wide region where small-scale yielding holds) appears as a sharp, well-focused slip band or shear zone (Fig. 12c), which is often associated with a fast growing crack. As the crack tip approaches a triple junction, the multitude of additional slip systems presented by adjacent grains diffuses and spreads the intensity of the plasticity, often resulting in a bifurcated or multi-branched plastic zone (Fig. 12a and b), especially in Fig. 12b, where the plastic zone is much more strongly split, or bifurcated than in Fig. 12a. This stronger bias of the plastic zone to the left is considerable, even though not enough to cause the crack to change direction, but greatly reduces the advance of the right-going branch. This "virtual crack branching" may effectively lower the local crack-driving force and provide the impetuous for crack deflection, noticing that the crack-growth rate in Fig. 12b is considerably lower than those in Fig. 12a and c, while the driving force $\Delta K_{cor}$ in Fig. 12b is only slightly lower.

In addition, it is interesting to observe that local crystal orientation within single grains due to the plastic deformation ahead of the crack tip are predicted by the finite-ele-

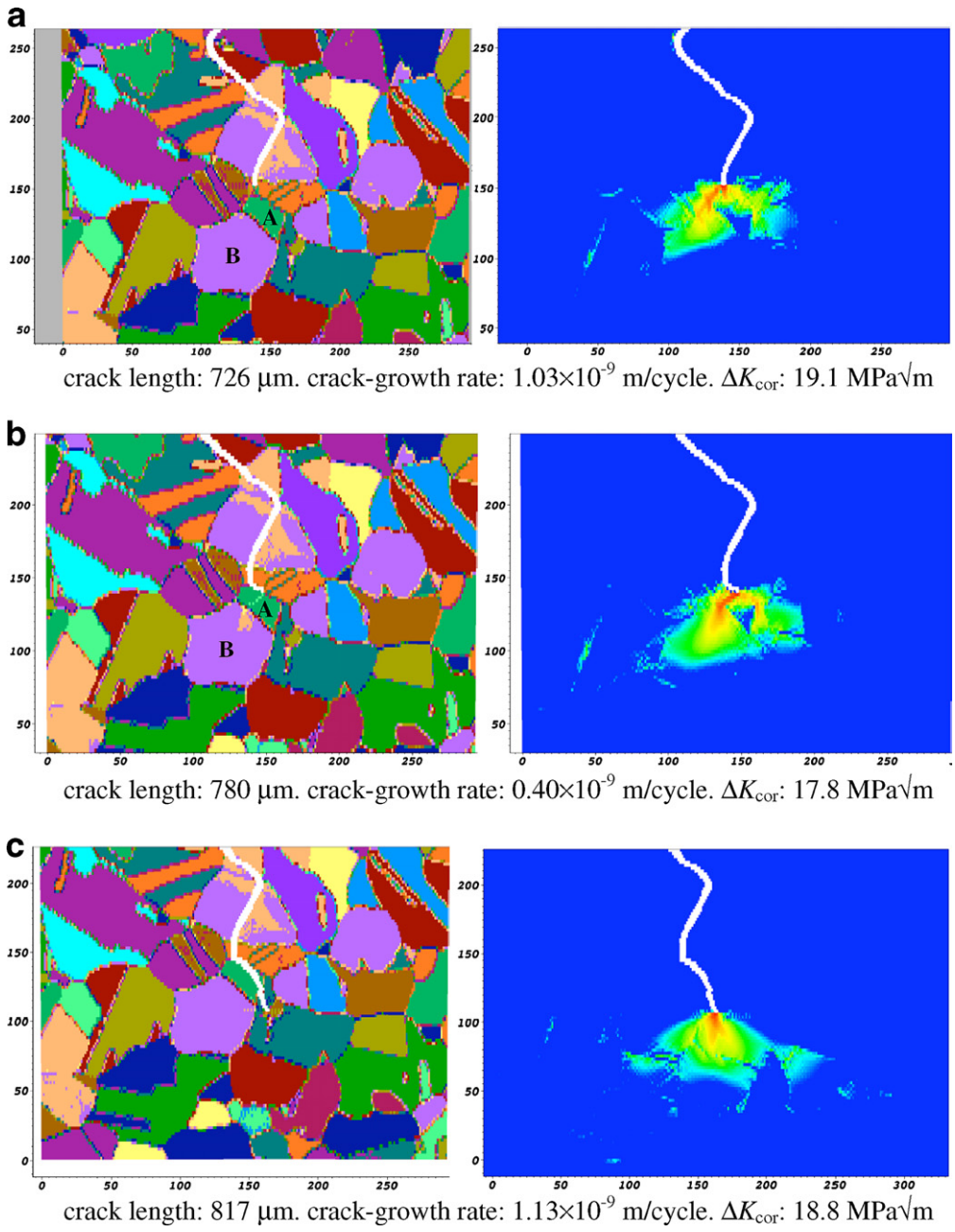


Fig. 12. EBSD characterization (left) and corresponding plastic-zone profile (right) in front of the crack tip in three consecutive measurements during the small crack propagation (scale in micrometers). Of note is that where the plastic zone becomes bifurcated (e.g., in (b)), a decreased in crack-growth rate is seen. Local changes in crystal orientation in grain "A" and grain "B", predicted by the finite-element analysis, are well correlated with the EBSD data.

ment simulation, (i.e., notice the color change in the grain "A" and "B" shown in Fig. 12b as compared to Fig. 12a). The apparent disappearance of this region in Fig. 12c is due to the manner in which the simulations were conducted. The simulations were performed by "inserting" the crack geometry into the grain-boundary structure with subsequent monotonic loading and therefore do not capture the details of the fatigue process and crack growth. The calculations do provide an estimate of the distribution and relative intensity of the stress and plastic strain fields as modulated by the local microstructure.

In general, the point-to-point deviation of the local crack-driving force ($\Delta K_{cor}$) for small cracks calculated in the finite-element simulations is on the order of 10% and can be as large as 16% (i.e., $\Delta K_{cor}$ of left vs. right crack tips in Table 2) when compared to conventional stress-intensity estimates. This unaccounted variation in driving force should be considered when examining the apparent local scatter in observed crack-growth rates. Assuming Paris-law-type behavior, these variations in driving force could further amplify the variability in growth rate, depending upon the value of the exponent. The variability in the

observed crack-growth rate can be roughly divided into two categories: factor of two or so fluctuations (''small fluctuations'', left box in Fig. 11) and order of magnitude variations (''large fluctuations'', right box in Fig. 11 and left crack-tip data). The magnitudes of local changes in driving force, e.g., 5–15% variations in applied $K$ due to microstructure, appear to be consistent with the small fluctuations in growth rates (left box in Fig. 11). With respect to the large fluctuations, an interesting observation is that in all cases where significant crack deflection occurred, a concomitant large fluctuation in crack-growth rate was observed (right box in Fig. 11 and left crack-tip data). The finite-element simulations suggest that crack deflection may be related to a redistribution of the plastic-zone intensity at the crack tip in the neighborhood of triple junctions. Such changes can be observed in Figs. 12a–c, where a small kinking event occurs in Fig. 12b. The crack-growth rate is first large (Fig. 12a), then smaller (Fig. 12b), and then increases again (Fig. 12c). The change in applied $K$ is ~6% while the change in crack-growth rate is ~280%, clearly orders of magnitude different (right box, Fig. 11). The finite-element simulations suggest that the local microstructure modulates the intensity of the local plastic zone, resulting in ''virtual crack branching'' of the nascent crack tip, thereby reducing the effective driving force by diffusing the local plastic-strain concentration.

## 5. Conclusions

Based on an experimental and numerical study of the role of grain-boundary character in influencing the predominantly transgranular propagation of microstructurally small surface cracks in a $\gamma/\gamma'$ nickel-base superalloy ME3 at ambient temperatures, the following conclusions can be made:

1. Grain-boundary-engineered microstructures, with a 40% increase in the fraction of special boundaries as compared to as-received microstructures (i.e., 41% vs. 28%), displayed only a marginal (~2–3%) increase in $10^8$-cycle endurance strength when compared at similar grain size. Fine-grained (1.3 μm) as-received microstructures, however, displayed a larger (~7%) increase in endurance strength when compared to coarse-grained (15 μm) as-received structures.
2. Measured fatigue thresholds for small (~10–900 μm) surface cracks were considerably lower ($\sim 5\ \mathrm{MPa}\sqrt{\mathrm{m}}$) than those for corresponding large (8–20 mm) through-thickness cracks. However, with respect to the role of grain-boundary engineering, there was little discernable overall effect of an increased fraction of special boundaries on the growth rate and threshold behavior of these small cracks.
3. Grain boundaries provide an impedance to the predominantly transgranular propagation of small surface cracks. Specifically, boundaries with higher misorientations on average tend to cause larger crack deflections and result in larger crack-growth retardations. However, at a fixed grain-boundary misorientation angles, special boundaries are no more effective than random boundaries in impeding transgranular small crack growth.
4. Due to their large misorientations ($\Delta\theta \sim 60°$), $\Sigma 3$ twin boundaries were found to be particularly effective at locally retarding such small crack extension.
5. Corresponding numerical simulations of such small-crack growth suggest that these measured perturbations in crack-growth rates are well associated with fluctuations in the effective crack-driving force and the profile of the plastic zone near the crack tip, which is significantly affected by the local microstructure, in particular the presence of grain boundaries and triple junctions.

## Acknowledgements

This work was supported by the US Air Force Office of Scientific Research under Grant No. F49620-02-1-0010. Part of this work was performed under the auspices of the US Department of Energy by the University of California, Lawrence Livermore National Laboratory under Contract No. W-7405-Eng-48. The authors thank Dr. Peter Kantzos at NASA Glenn and Drs. Ken Bain and Deborah Demania at GE Aircraft Engines for supplying the ME3 alloy, Lan T. Nguyen for specimen preparation, and Drs. J.J. Kruzic and R.K. Nalla for their assistance with the mechanical testing.

## References

[1] Report of the AdHoc Committee on Air Force Aircraft Jet Engine Manufacturing & Production Processes USAFSAB, SAF/AQQS: Washington (DC): The Pentagon; 1992.
[2] Chang JCI. Air Force Office of Scientific Research, Bolling AFB, Washington (DC); 1996.
[3] Cowles BA. Int J Fract 1996;80:147.
[4] Suresh S, Ritchie RO. Intl Matls Rev 1984;29:445.
[5] Ritchie RO, Lankford J. Mater Sci Eng 1986;84:11.
[6] Lankford J. Fatigue Eng Mater 1982;5:233.
[7] Ravichandran KS, Ritchie RO, Murakami Y, editors. Small fatigue cracks: mechanics, mechanisms and applications. Oxford (UK): Elsevier; 1998.
[8] Newman JC. Prof Aero Sci 1998;34:347.
[9] Zhang YH, Edwards L. Mater Sci Eng A 1994;188:121.
[10] Zhai T, Wilkinson AJ, Martin JW. Acta Mater 2000;48:4917.
[11] Watanabe T. Res Mech 1984;11:47.
[12] Grimmer H, Bollmann W, Warringt Dh. Acta Crystallogr A 1974;30:197.
[13] Brandon DG, Ralph B, Ranganathan S, Wald MS. Acta Metall 1964;12:813.
[14] Kumar M, Schwartz AJ, King WE. Acta Mater 2002;50:2599.
[15] Palumbo G, Aust KT. Scripta Metall 1988;22:847.
[16] Palumbo G, Aust KT. Acta Metall Mater 1990;38:2343.
[17] Palumbo G, King PJ, Aust KT, Erb U, Lichtenberger PC. Scripta Metall Mater 1991;25:1775.
[18] Crawford DC, Was GS. Metall Trans A 1992;23:1195.
[19] Lin P, Palumbo G, Erb U, Aust KT. Scripta Metall Mater 1995;33:1387.
[20] Palumbo G, Aust KT. Can Metall Quart 1995;34:165.

[21] Lehockey EM, Palumbo G, Lin P, Brennenstuhl A. Metall Mater Trans A 1998;29:387.
[22] Dave VR, Cola MJ, Kumar M, Schwartz AJ, Hussen GNA. Welding J 2004;83:1S.
[23] Was GS, Alexandreanu B, Andresen P, Kumar M. Mater Res Soc Proc 2004;819:87.
[24] Lehockey EM, Palumbo G, Lin P. Metall Mater Trans A 1998;29:3069.
[25] Gao Y, Kumar M, Nalla RK, Ritchie RO. Metall Mater Trans A 2005;36:3325.
[26] Gabb T, Telesman J, Kantzos P, O'Connor K. NASA TM-2002-211796; 2002.
[27] Newman JC, Raju IS. Eng Fract Mech 1981;15:185.
[28] Kumar M, King WE, Schwartz AJ. Acta Mater 2000;48:2081.
[29] Schwartz AJ, Kumar M, King WE. MRS Symp Proc 2000;586:3.
[30] Schuh CA, Kumar M, King WE. Acta Mater 2003;51:687.
[31] Cho JH, Rollett AD, Oh KH. Metall Mater Trans A 2005;36:3427.
[32] Lei Y. Eng Fract Mech 2005;72:577.
[33] Gourgues A. Mater Sci Tech 2002;18:119.
[34] Garrett GG, Knott JF. Acta Metall 1975;23:841.
[35] Peralta P, Kickerson R, Dellan N, Komandur K, Jameel MA. J Eng Mater Tech 2005;18:119.